

Evolution of deep-water waves under wind forcing and wave breaking effects: Numerical simulations and experimental assessment



Zhigang Tian^{a,b}, Wooyoung Choi^{a,c,*}

^a Division of Ocean Systems Engineering, Korea Advanced Institute of Science and Technology (KAIST), Daejeon 305-701, Republic of Korea

^b Naval Architecture Department, Exmar Offshore Company, Houston, TX 77042, USA

^c Department of Mathematical Sciences, Center for Applied Mathematics and Statistics, New Jersey Institute of Technology, Newark, NJ 07102, USA

ARTICLE INFO

Article history:

Received 4 January 2012

Received in revised form

11 February 2013

Accepted 1 April 2013

Available online 11 April 2013

Keywords:

Water waves

Wave breaking

Wind forcing

ABSTRACT

The evolution of two-dimensional dispersive focusing wave groups in deep water under wind forcing and wave breaking effects is investigated numerically and measurements collected from wind-wave experiments are used to evaluate the numerical simulations. Wind forcing is modeled by introducing into the dynamic boundary condition a surface slope coherent pressure distribution, which is expressed through Miles' shear instability theory and Jeffreys' sheltering model. To activate Jeffreys' model in simulating waves evolving under wind forcing, an air flow separation criterion depending on wind speed and wave steepness is proposed. Direct comparisons of the measurements and the simulations are made by including the wind-driven current in the simulations. To simulate breaking waves, an eddy viscosity model is incorporated into a system of nonlinear evolution equations to dissipate wave energy and to predict surface elevation after breaking. For wave groups under no wind action, the eddy viscosity model simulates well the energy dissipation in breaking waves and predicts well the surface elevation after breaking. Under the weaker wind forcing condition, after consideration of the wind-driven current, the numerical model produces satisfying predictions. As the wind forcing becomes stronger, the disparity between the experiments and the simulations becomes more evident while the numerical results are still regarded as acceptable. The relative importances of the Miles' and the Jeffreys' models for waves under wind forcing are discussed through additional numerical tests.

© 2013 Elsevier Masson SAS. All rights reserved.

1. Introduction

Accurate prediction of the evolution of nonlinear water waves is crucial for ships and offshore structures operating in severe sea states where extreme events such as freak waves could occur. As ocean waves are conventionally assumed to be random, their description is typically through quantification of statistically relevant properties, e.g. wave spectrum, and the phase of individual waves is disregarded. However, the phase-averaging approach cannot describe local wave kinematics and may not provide enough information to meet engineering design requirements. Recently, much progress has been made towards deterministic prediction of ocean waves using phase-resolving nonlinear wave models (e.g. [1,2]).

Deterministic prediction of ocean waves is a very challenging task as the wavefield evolution involves many complicated physical processes, such as wave-wave, wind-wave, and wave-current

interactions. Wind blows over the sea surface and transfers momentum and energy to surface waves through air-sea interaction. The generated waves may grow under continuous wind forcing and their energy redistributes among different components through nonlinear wave-wave interaction. Wave breaking also occurs and dissipates wave energy, part of which may contribute to the generation of surface current. Some of the physical processes involved, e.g. wind forcing and wave breaking, are not well understood yet and, hence, the development of proper models remains challenging.

For the prediction of nonlinear water wave evolution, a pseudo-spectral method using asymptotic expansion was developed by West et al. [3]. This method when combined with fast Fourier transform [4] has been shown to be an accurate and effective tool to simulate non-breaking irregular waves, e.g. in [5,6]. Recently, the pseudo-spectral method has been further developed and applied to simulate energy dissipation in breaking waves [7,8] and to predict wave evolution under wind action [9,10].

Simulation of energy dissipation due to wave breaking can be achieved through an eddy viscosity model based on boundary layer approximation and dimensional analysis [7]. This model is further developed so that it can be implemented automatically in

* Corresponding author at: Division of Ocean Systems Engineering, Korea Advanced Institute of Science and Technology (KAIST), Daejeon 305-701, Republic of Korea.

E-mail address: wychoi1111@gmail.com (W. Choi).

simulation of breaking wave groups [8]. In the refined model, three sets of correlations between pre-breaking local wave parameters and post-breaking time and length scales are identified according to experimental measurements. These connections are used to predict post-breaking scales and to estimate the magnitude of the eddy viscosity based on the pre-breaking parameters when wave breaking occurs, indicated by a critical surface slope S_c ($=0.95$ in their numerical simulations). The model was demonstrated to simulate well the total energy dissipation due to wave breaking in comparison with laboratory experiments; in addition, the surface elevation after wave breaking is predicted well for dispersive focusing wave groups and irregular waves characterized initially by the JONSWAP spectrum.

The influence of wind on the evolution of nonlinear water waves can be modeled by introducing an external surface pressure in the dynamic free surface boundary condition. One model assumes that the wind induced pressure is in phase with the wave surface slope and depends on the friction velocity on the surface due to the wind forcing [11]. This model originates from Miles' shear flow instability theory [12] for wave generation and assumes no air flow separation. With this simple model, Banner and Song [11] studied the wind forcing effect on the performance of a wave breaking criterion based on local energy convergence rate. In addition, Kalmikov [2] conducted the deterministic prediction of the evolution of nonlinear water waves under wind forcing using a spectral method. Neither of the numerical studies provided experimental assessment of the performance of this wind forcing model.

An alternative model for wind forcing is based on Jeffreys' sheltering hypothesis [13]. This model also involves a wave slope coherent pressure on the free surface, but is supposed to be applicable only to waves over which air flow separates [9,10]. Although it has been applied to study extreme waves under wind action, the sheltering model is still debatable and has to be tested carefully with experiments. Touboul et al. [9] are the first to use the sheltering model to study the generation of freak waves from dispersive focusing wave groups under wind forcing. Due to the focus of their study, as well as the high initial steepness of their wave groups, reproducing their experiments numerically was not trivial and only limited assessment of performance of the sheltering model was performed. Their subsequent study [10] investigated the wind forcing effect on extreme waves. The influence of wind on possibly sustaining extreme waves due to air flow separation is discussed through experimental observations and numerical simulations with a similar sheltering model. Yan and Ma [14] conducted CFD simulations on the interaction of freak waves and wind and revealed that the sheltering hypothesis may not describe the pressure over freak waves accurately.

Even if the sheltering model is accepted as a physically adequate one, a condition under which air flow separation occurs has to be known before this simple model is adopted in numerical simulations. In fact, the determination of a criterion for air flow separation over water waves has been an interesting subject due to its importance in the wind-wave interaction process. Wu [15] proposed that air flow separation over water waves with a following wind occurs when the friction velocity is greater than the wave phase velocity. Later, Banner and Melville [16] argued that air flow separation occurs only in the presence of breaking waves. They managed to observe air flow separation over a steady breaking crest by means of smoke visualization and also a non-separated flow over an unbroken, steady wave. However, Kawai and Weissman [17,18] suggested the possibility of air flow separation over non-breaking wind waves and supported their arguments with flow visualization experiments. Recently, Kharif et al. [10] used a device composed of hot and cold wires to detect air flow separation over frequency focusing wave groups and a

critical local wave slope, $(\partial\zeta/\partial x)$, close to 0.35 was determined to indicate the onset of air flow separation. Kharif et al. [10] further noted that the air flow separation was accompanied generally by breaking waves.

In numerical studies, Touboul et al. [9] chose a critical slope $(\partial\zeta/\partial x) = 0.5$ to predict the onset of air flow separation. No experimental support is provided for this criterion. Kharif et al. [10] adopted a critical local wave slope, $\partial\zeta/\partial x \sim 0.35$ to indicate air flow separation onset for their numerical simulations. The discrepancy in the critical slope for air flow separation may arise from the different wind forcing conditions considered in these studies. Therefore, an improved criterion, possibly depending on both local wave slope and wind speed, for the application of the sheltering model shall be proposed.

Overall, comprehensive experimental evaluation of the above-mentioned numerical models for the evolution of nonlinear water waves under wind forcing is sparse. In this study, as a first step towards developing more robust wind-wave interaction models, we conduct laboratory experiments of nonlinear water waves under wind action to evaluate the applicability of two existing wind forcing models, i.e. Miles' and Jeffreys' models, and to assess their performance. In addition, to resolve the observed inconsistency on the air flow separation criteria adopted in previous numerical simulations, a separation criterion considering both wind speed and wave steepness is proposed. The rest of the study is organized as follows. After this introduction, a detailed description of the numerical models is presented. Section 3 provides experimental set-up, wave group generation, and wind forcing conditions. Experimental and numerical results, as well as their comparison, are given in Section 4. The last section summarizes main findings and concludes this study.

2. Numerical models

For the prediction of the evolution of water waves, West et al. [3] developed a nonlinear wave model based on asymptotic expansion, where wave dynamics is governed by the following system of nonlinear evolution equations for the surface elevation, ζ , and the velocity potential Φ , on the free surface [3,19,20]:

$$\frac{\partial\zeta}{\partial t} = \sum_{n=1}^N Q_n[\zeta, \Phi] \quad \text{and} \quad \frac{\partial\Phi}{\partial t} = \sum_{n=1}^N R_n[\zeta, \Phi]. \quad (1)$$

Here Q_n and R_n are two nonlinear operators that can be written explicitly through recursion formulas and N is the order of nonlinearity at which the original infinite series on the right-hand sides are truncated. This model can be solved numerically using an efficient pseudo-spectral method based on Fast Fourier Transform and is known to be accurate and effective to predict non-breaking irregular wave evolution.

However, the simulation cannot provide reliable predictions when wave breaking occurs. In the presence of wave breaking, the wave-induced flow near the water surface becomes turbulent and multi-phased, and no analytical description of the flow is possible. Nevertheless, the wave breaking effect has to be considered for a reasonable prediction of the evolution of water waves. In addition, modeling the wind forcing effect is necessary for nonlinear waves under wind action which transfers energy to waves, induces wave growth, and affects significantly the wave dynamics. To model these effects, the nonlinear evolution equations given by (1) are modified to

$$\begin{aligned} \frac{\partial\zeta}{\partial t} &= \sum_{n=1}^N Q_n[\zeta, \Phi] + D_\zeta[\zeta, \Phi] \quad \text{and} \\ \frac{\partial\Phi}{\partial t} &= \sum_{n=1}^N R_n[\zeta, \Phi] + D_\Phi[\zeta, \Phi] + \Pi[\zeta, \Phi], \end{aligned} \quad (2)$$

where D_ζ and D_Φ are energy dissipative terms due to wave breaking and Π may represent a pressure term induced by the action of wind over steep or breaking waves.

2.1. Wave breaking model

In our previous studies [7,8], we developed an eddy viscosity model to simulate energy dissipation in two-dimensional unsteady plunging breakers using a boundary layer approach and dimensional analysis:

$$D_\zeta [\zeta, \Phi] = 2\nu_{\text{eddy}} \frac{\partial^2 \zeta}{\partial x^2} \quad \text{and} \quad D_\Phi [\zeta, \Phi] = 2\nu_{\text{eddy}} \frac{\partial^2 \Phi}{\partial x^2}, \quad (3)$$

where the eddy viscosity ν_{eddy} depends on breaking strength and can be estimated through time and length scales associated with a breaking event:

$$\nu_{\text{eddy}} = \alpha \frac{H_{br} L_{br}}{T_{br}}. \quad (4)$$

Here, T_{br} is defined as the time when the wave crest begins to fall to the time when the surface disturbance front is no longer obvious; L_{br} is the distance from incipient breaking to where the obvious surface disturbance ends; H_{br} refers to the falling crest height [21]; α is a proportional constant and $\alpha = 0.02$, as determined in [7]. We stress that our wave breaking model uses a constant eddy viscosity over a finite spatial range of L_{br} during a finite period of T_{br} for a given wave breaking event. However, the eddy viscosity ν_{eddy} is determined dynamically and varies depending on the breaking strength of specific breaking events.

Note that an alternative formulation for the estimation of the eddy viscosity was proposed by Drazen and Melville [22], who conducted measurements of turbulent mixing introduced by unsteady breaking waves. While their interest lies in the eddy viscosity of the turbulence generated by a wave breaking event (timescale of tens of wave periods), this study focuses on modeling energy dissipation due to wave breaking within one or two wave periods subsequent to breaking. Details of their study can be found in [22]. Notice that their eddy viscosity term has not been modeled for any deterministic wave model for the prediction of post-breaking wave evolution and, therefore, a direct comparison between the two eddy viscosity models is not straightforward.

To implement the eddy viscosity model in numerical simulations, Tian et al. [8] used a critical surface slope $S_c = (\partial \zeta / \partial x)_c = 0.95$ to indicate wave breaking so that the eddy viscosity model is put into effect and three sets of correlations between pre-breaking parameters and post-breaking scales (i.e. T_{br} , L_{br} and H_{br}) to estimate the magnitude of the eddy viscosity, as shown below:

$$\kappa_b L_{br} = 24.3S_b - 1.5, \quad (5)$$

$$\omega_b T_{br} = 18.4S_b + 1.4, \quad (6)$$

$$\kappa_b H_{br} = 0.87R_b - 0.3. \quad (7)$$

Here, S_b is a local wave steepness; κ_b is a local wavenumber based on zero crossings and ω_b is the corresponding angular frequency according to the linear dispersion relation; $R_b = L_b/L_c$ is a horizontal wave crest asymmetry. Here L_b is the distance between the crest tip and the zero-crossing point immediately behind it and L_c is the distance between two consecutive zero-crossing points adjacent to the breaking crest. These parameters can be determined with a simulated surface profile just prior to wave breaking, indicated by the critical surface slope S_c exceeding 0.95 in the simulations. Details regarding the definitions and the implementation scheme are referred to the previous work [8].

2.2. Wind forcing model

A physics-based model for wind forcing effect on steep waves in terms of local wave characteristics remains to be developed.

However, a typical approach to simulate the wind forcing effect is to introduce an external surface pressure distribution in phase with the wave surface slope, i.e. wave slope coherent pressure, in the dynamic free surface boundary condition. In this case, $\Pi [\zeta, \Phi] = P_{wind} / \rho_{water}$, where P_{wind} is the wave slope coherent pressure due to wind. One of the models for P_{wind} is expressed with the following equation [12,11,2]:

$$P_{wind} = \beta \rho_a u^{*2} \frac{\partial \zeta}{\partial x}, \quad (8)$$

where β is a coefficient that remains to be determined and u^* is the friction velocity on the water surface due to wind. Coefficient β may be evaluated through theoretical analysis based on Miles' shear flow instability theory [12]. Alternatively the coefficient can be determined through the observed wave growth rate in experiments and field measurements; e.g. Banner and Song [11] estimated that β is approximately 32.5.

A second form of the wave slope coherent pressure originates from the so-called Jeffreys' sheltering hypothesis [13]. The sheltering hypothesis was developed to study the wave generation by wind. The theory assumes air flow separation over waves and that wave generation is mainly due to wave slope coherent pressure. Recently, the hypothesis was applied to model the strong wind forcing effect on steep water waves due to air flow separation [9,23,10]. In this model, the forcing term is written as

$$P_{wind} = s \rho_a (U_0 - c)^2 \frac{\partial \zeta}{\partial x}, \quad (9)$$

where the sheltering coefficient $s = 0.5$ is reported in [9,10], ρ_a is air density, U_0 is the wind speed, and c is the local wave phase velocity, which is determined through a local wavenumber and the linear dispersion relation. The local wavenumber is defined by consecutive zero-crossings of the surface elevation. While the two forcing terms given by (8) and (9) are similar in the sense that both are proportional to the wave slope, we should remark that Jeffreys' model is applied only when the condition for flow separation is met, as discussed in Section 4.

We note that the wind friction velocity measured in a wave tank is approximately 5% of the wind speed, i.e. $u^*/U_0 \sim 0.05$ (e.g. [24,29]). In the case of slow waves propagating under fast wind, $U_0 \gg c$, the ratio of P_{wind} from the two theories may be estimated as $(P_{wind})_{Jeffreys} / (P_{wind})_{Miles} \sim 400s/\beta \sim 6$, where $s = 0.5$ and $\beta = 32.5$ are used. However, one has to consider the fact that air flow separation is highly unsteady; it may occur rapidly and only persist for a very short time [25,26]. Therefore, the evaluation of the overall effects from air flow separation on wave evolution is non-trivial [27]; in addition, the relative importance of the two mechanisms should depend on specific wind forcing conditions. Touboul et al. [9] conducted analysis of the characteristic time scales associated with wind forcing and found that the sheltering mechanism plays a more important role in their study (wind speed varies from 4 to 8 m/s and peak wave frequency is 1 Hz).

3. Experiments

Experiments are performed at the Korea Advanced Institute of Science and Technology (KAIST) in a two-dimensional wind-wave tank with glass walls and removable, transparent plastic ceiling panels. The tank is 15 m long, 1.5 m wide, and has a water depth as used of 0.54 m. A servo-controlled piston-type wavemaker and auxiliary electronics are located at one end of the tank and used to generate water waves. At the same end, a twin-fan blower is installed on the top of the tank to generate following wind. A maximum wind speed of 10 m/s can be produced. The distance between the calm water surface and the ceiling panels (i.e. air passage gap) remains 0.45 m in the experiments. At the other end

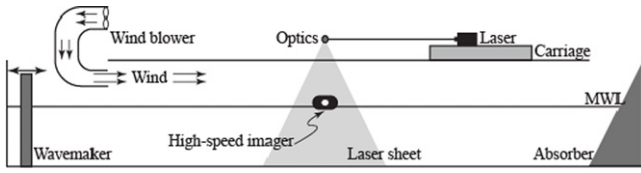


Fig. 1. Illustration of the two-dimensional wind-wave tank (not to scale) and measurement devices.

Table 1

Specified parameters for the wave groups. DF indicates dispersive focusing wave groups. f_c is the center wave frequency and $\Delta f/f_c$ is the frequency bandwidth specified. f_p is the spectral peak frequency. $\varepsilon = Nk_n a_n$ is the initial wave steepness specified in wave generation ($N = 128$). Under no wind action, DF 1 is a non-breaking group and DF 2 is a breaking one. Note that DF 1 remains non-breaking under all wind forcing conditions.

Wave group	f_c (Hz)	f_p (Hz)	$\Delta f/f_c$	$\varepsilon = Nk_n a_n$
DF 1	1.7	1.1	0.824	0.25
DF 2	1.7	1.1	0.824	0.57

of the tank, a wave absorber made of loose nets and stainless steel grids reduces wave reflection. A movable carriage is installed on the top of the tank and provides a work platform. Fig. 1 illustrates a sketch of the experimental set-up.

3.1. Wave group generation

Dispersive focusing wave groups are generated in the experiments, where the surface elevation, ζ , is described as

$$\zeta(x, t) = \sum_{n=1}^N a_n \cos(k_n x - \omega_n t - \phi_n). \quad (10)$$

Here, a_n is the amplitude of the n th wave component; k_n is the wavenumber; $\omega_n = 2\pi f_n$ is the angular frequency and f ranges from 1.0 to 2.4 Hz (center frequency $f_c = 1.7$ Hz and frequency bandwidth $\Delta f = 1.4$ Hz); $N = 128$ is the total number of frequency components; ϕ_n is the initial phase to be determined. In addition, x is the horizontal distance downstream of the wavemaker with $x = 0$ being the mean position of the wavemaker; time t is relative to the initial motion of the wavemaker (i.e. $t = 0$). The linear dispersion relation is used to relate ω_n and k_n . Wave steepness, $\varepsilon_n = k_n a_n$, for each of the components is the same and can be adjusted.

The phase ϕ_n is determined so that the wave groups focus at specified time t_b and location x_b , i.e. $\cos(k_n x_b - \omega_n t_b - \phi_n) = 1$. Therefore, $\phi_n = k_n x_b - \omega_n t_b + 2\pi m$, where $m = 0, \pm 1, \pm 2, \dots$. By substituting ϕ_n into (10) and setting $x = 0$, the surface elevation at the wavemaker can be obtained as

$$\zeta(0, t) = \sum_{n=1}^N a_n \cos[-k_n x_b - \omega_n(t - t_b)]. \quad (11)$$

To generate the input signal to the wavemaker, a transfer function between the wavemaker stroke and the surface elevation is first determined in calibration tests; the transfer function is then applied to Eq. (11) to obtain the input to the wavemaker. Note that, in the calibration tests, measurements of the surface elevation in the transverse direction across the wave tank showed good two-dimensionality of generated sinusoidal waves and focusing wave groups. To avoid an abrupt motion of the wavemaker and the development of noise in the tank, such as the cross tank waves and reflected waves from the absorber, a window function is applied to the produced input signal. Key parameters of these wave groups are listed in Table 1.

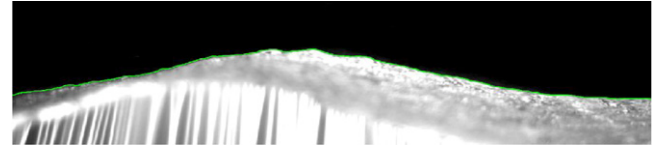


Fig. 2. A sample image (resized) and the detected air-water interface (solid line) for a dispersive focusing group under wind condition $U_0 = 5$ m/s.

3.2. Surface elevation measurement

We attempt to measure the surface elevation with capacitance-type wave probes. However, it is found that the wave probe supporting rod is disturbed and vibrating in the presence of wind in the tank. Therefore, wave probe measurements may be rendered inaccurate by the disturbance. Alternatively, surface elevation is measured through high-speed imaging.

In the experiments, a 15 W DPSS laser is used as the light source for illumination. A thin laser light sheet is generated through a series of optics and is directed downward into the water, in which fluorescent dye (Rhodamine 6G) is dissolved to improve the illumination. A high-speed imager (Phantom V9.1 with 12 GB internal memory) mounted outside of the tank is used to capture the surface elevation and to facilitate the observation of evolution of the wave groups. The imager, equipped with a 50 mm focal length Nikon lens, is positioned in front of the tank with its axis oriented slightly downwards for a better view of the illuminated air-water interface. Images are captured at 200 frames per second (fps) and the exposure time is set to one millisecond. The size of the field of view depends on specific set-ups at different locations along the tank, but the length is approximately 50 cm (1600 pixels) and the width is adjustable (approximately 25 cm and 800 pixels). Using a precise planar target with known spacing, the spatial resolution is determined and the image distortion is shown to be negligible. The devices and the measurement set-up are illustrated in Fig. 1.

For the imaging at a wave station along the tank, the recording duration is long enough to allow the entire wave group to pass by the wave station. Each of the snapshots is then processed with the Image Processing Toolbox in MATLAB and the air-water interface is determined through edge detection functions based on the Canny method. Fig. 2 provides an example of a snapshot and the detected water surface. Finally, the surface elevation as a function of time can be obtained by applying the same processing procedure to the series of the snapshots. Note that the strategy used to extract surface elevation from the imaging is sufficiently accurate for low and moderate steep waves; however, for very steep waves and/or in the presence of wave breaking, spurious surface can be detected due to illumination related issues. Therefore, a filter (i.e. smooth function with robust local regression method in MATLAB) is applied to the temporal surface elevation to eliminate these obvious spurious surface elevations. Fig. 3 shows the temporal surface elevation of the two wave groups measured at 2.84 m downstream of the wavemaker.

3.3. Wind forcing conditions

In the experiments, the twin-fan blower is used to generate following wind. The wind entry is located at 1.49 m downstream of the wavemaker, i.e. $x = 1.49$ m (hereafter, x_f is defined as the distance relative to the wind entry and $x_f = x - 1.49$ m). In each test, before the operation of the wavemaker and any data collection, the blower is run for at least 10 min so that a statistical equilibrium state of the wind-generated waves can be achieved in the tank.

We considered three wind forcing conditions, i.e. mean free stream wind speed $U_0 = 1.4, 3.2$, and 5.0 m/s. The mean wind

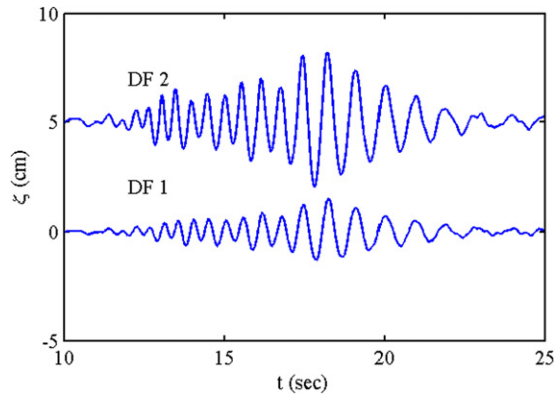


Fig. 3. Surface elevations measured at 2.84 m downstream of the wavemaker. No wind forcing is applied. For clarity, an increment of 5 cm is applied in the ordinate to separate measurements of the two wave groups.

speed is measured with a portable anemometer (Flowatch, JDC Instruments) at the centerline (transverse direction of the wave tank) 24 cm above the calm water level at a fetch of 4.87 m. Notice the wind speed is measured at a vertical location where the wind profile becomes uniform in the vertical direction. Therefore, its distance from the calm water level is not so crucial as long as it is far away from the edge of turbulent boundary layer and the variation of the mean wind speed is relatively little. The averaging period for the measurement is 30 s and multiple readings are obtained and averaged. Fig. 4 presents the mean free stream wind speed as a function of fetch (i.e. distance downstream of the wind entry) and the transverse mean wind velocity profile across the tank. Clearly, for a given wind condition, the mean wind velocity decreases significantly from the wind entry to about $x_f = 2.5$ m, after which it remains approximately constant. In the transverse direction, the mean wind velocity remains approximately constant in the middle section ($y \leq \pm 40$ cm) of the tank.

Vertical mean wind velocities as a function of distance above the mean water surface are provided in Fig. 5. As shown, the air flow is not fully developed at the shorter fetch ($x_f = 1.87$ m) and the vertical mean velocity profile is significantly different from that measured at the longer fetches. We examined the velocity profiles close to the mean water surface ($z \leq 15$ cm) at the longer fetches ($x_f = 4.87$ m and 7.87 m) and found that they follow well the so-

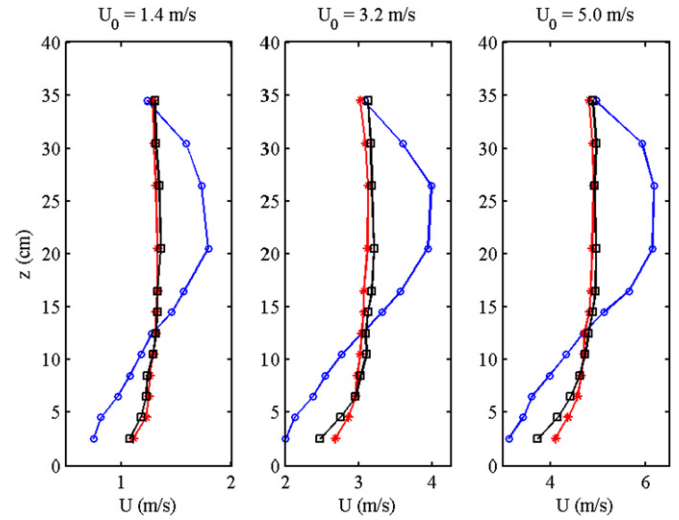


Fig. 5. Vertical mean wind velocity profiles as a function of distance above the mean water surface (i.e. $z = 0$). The results are measured in the middle of the tank in the transverse direction at three different fetches, i.e. $x_f = 1.87$ m (circles), 4.87 m (asterisks), 7.87 m (squares).

called logarithmic law:

$$\frac{u(z)}{u^*} = \frac{1}{\kappa} \ln \left(\frac{z}{z_0} \right),$$

where the von Karman constant κ is given by $\kappa = 0.41$ and z_0 is the roughness length which can be estimated through the measured vertical velocity profile. The measured profiles are then used to determine the friction velocities, as provided in Table 2. The estimations are comparable with those in [26,28] despite the difference of the experimental facilities and the wind generation technique. In addition, the ratio of the friction velocity to the mean speed, $u^*/U_0 \sim 0.041$ – 0.056 at the far downstream location ($x_f = 7.87$ m), where the air flow and wind generated waves are fully developed, is consistent with typical measurements found in a wave tank (e.g. [24,29]).

These wind forcing conditions are applied to the focusing wave groups and observations on the evaluation of the groups are made. The experimental results will be used to evaluate the performance of existing numerical models of wind forcing and wave breaking effects.

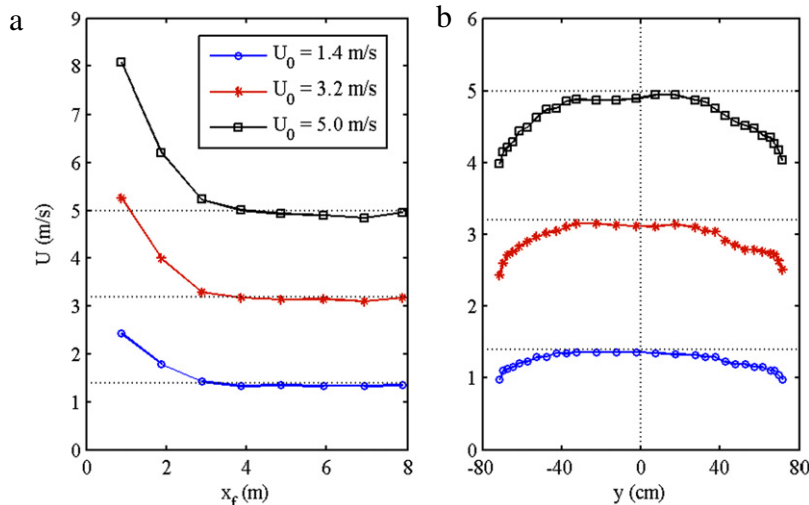


Fig. 4. (a) Mean free stream wind velocity as a function of fetch and (b) transverse mean wind velocity profile across the tank. Data provided in (a) are measured at 24 cm above the mean water surface at the center of the tank in the transverse direction; (b) are measured at the same vertical distance at $x_f = 4.87$ m. y indicates the distance from the middle of the tank in the transverse direction.

Table 2

Estimated friction velocity (u^*) based on wind profile measurements (Fig. 4) and the logarithmic law, $\frac{u(z)}{u^*} = \frac{1}{\kappa} \ln\left(\frac{z}{z_0}\right)$. Here, the von Karman constant $\kappa = 0.41$. Note that only measurements close to the mean water surface ($z \leq 15$ cm) are used in the estimation.

U_0 (m/s)	u^* (m/s)	
	$x_f = 4.87$ m	$x_f = 7.87$ m
1.4	0.039	0.058
3.2	0.083	0.171
5.0	0.163	0.282

4. Numerical simulations and results

4.1. Simulation set-up

The wind forcing and wave breaking models, i.e. Eqs. (3), (8) and (9), are incorporated into the pseudo-spectral model given by Eq. (2) to simulate the evolution of two-dimensional water waves. In the code, the right-hand sides of Eq. (2) were truncated to the fifth order and the nonlinear evolution equations of the system were solved numerically with a pseudo-spectral method based on the fast Fourier transform (FFT) and a fourth-order Runge–Kutta method to integrate in time.

A brief description of the numerical simulation set-up and the generation of initial conditions are provided here while the details are referred to [8]. The simulations are conducted in a numerical wave tank 50 m long with the domain from 20 to 35 m corresponding to the physical wave tank. The numerical domain is discretized with 2^{12} points and a time step of 0.01 s is used in the simulations. The simulation period, T , is 40.95 s, which is of sufficient duration for the wave groups to completely pass the last wave station.

Using linear wave theory, initial conditions, i.e. spatial variation of the surface profiles and velocity potentials (from 0 to 20 m in the numerical domain) at the mean water level, are generated with surface elevation measurements at the first wave station (see Fig. 3). As discussed in [6], this initialization scheme based on linear theory introduces small errors to the velocity potential of an initial wavefield that is relatively linear. In addition, a five point moving average is applied to the measured surface elevation and only the first 256 Fourier modes (up to 6.25 Hz) are used in the initial condition generation. To match the surface elevation measured at the first wave probe, the first-order model without viscous effects is solved over the spatial domain up to the location of the first probe. In the remainder of the numerical tank, the fifth-order model with the wave breaking and wind forcing models is solved. In addition, an equivalent kinematic viscosity, $\nu_{eqv} = 5 \times 10^{-6}$ m²/s is applied to the free surface boundary conditions to account for the free surface damping and the frictional loss due to tank side walls and bottom. The equivalent viscosity is determined such that the total energy predicted in the simulations matches the measurements for the non-breaking wave group.

Dommermuth [30] showed that his high-order spectral wave model initialized with linear theory could excite spurious high frequency waves and nonlinear terms need to be adjusted to grow gradually over a finite time period. Combined with our domain decomposition technique to solve linear and nonlinear models in their respective domain, our initialization scheme based on linear theory guarantees numerical solutions for the surface elevation at the first wave probe location to match exactly with the corresponding laboratory measurements. This cannot be achieved with the adjustment technique suggested by Dommermuth [30]. Although our initialization scheme needs to be improved, we remark that our numerical solutions show excellent agreement with laboratory measurements in the absence of wind and wave breaking, as can be seen later, and, therefore, the simple initialization scheme based on linear theory is adopted for this study.

To simulate breaking waves under no wind action, the critical surface slope $S_c = 0.95$ is used to indicate wave breaking and the magnitude of the eddy viscosity is estimated with Eq. (4), in which the post-breaking scales are predicted with Eqs. (5)–(7). The pre-breaking wave parameters in these equations are determined with a simulated surface profile when the local surface slope just exceeds the critical one. In the presence of the wind forcing, waves may break at a reduced steepness [31] and the post-breaking time and length scales may demonstrate different characteristics from those under no wind action; however, the same breaking model is adopted to simulate breaking waves in wind forcing conditions in this study.

As for the wind forcing, the surface pressure distribution is applied from the position of the wind entry ($x = 1.49$ m in the physical tank, corresponding to 21.49 m in the numerical tank) to the end of the tank. Miles' model, i.e. Eq. (8) with $\beta = 32.5$, is used in the absence of air flow separation and the sheltering model, i.e. Eq. (9) with $s = 0.5$, is applied locally if air flow separation is predicted based on the flow separation criterion discussed in the following section.

4.1.1. Air flow separation over steep water waves

Previous attempts at the determination of a criterion for air flow separation typically focused on the local wave geometry only (e.g. wave steepness and surface slope); however, one may argue that a plausible separation criterion may depend on both wave steepness and wind forcing condition, as both play important roles in the wind–wave interaction. In recent field measurements, Donelan et al. [32] observed full air flow separation over non-breaking waves in a shallow lake and they argued that the air flow separation may depend on the force balance over the wave crests. The balance is as follows: the vertical gradient of pressure, proportional to $(U - c)(ka)^2$, shall match the centripetal acceleration, proportional to $(\partial^2 \zeta / \partial x^2)$, required to keep the streamlines in contact with the wave surface. Here, U is the wind speed measured at one half wavelength above the wave crest and $\partial^2 \zeta / \partial x^2$ is approximated with wave steepness, ka , based on deep water Stokes expansion. The study considered explicitly, for the first time, the wind speed effect on the air flow separation over water wave crests. More recently, Tian et al. [28] conducted flow visualization experiments and observed the air flow structure over mechanically generated waves. They identified conditions, i.e. proper combinations of local wave steepness and wind speed, under which air flow separation is likely to occur. The laboratory experimental results are consistent with the field measurements of Donelan et al. [32].

The data in [32,10,28] are reprocessed and plotted in Fig. 6. With the results, an air flow separation criterion is proposed and it is indicated with the blue solid line in the figure. The equation for the criterion is given as follows

$$\frac{(U_0 - c)}{c} \geq -59.3S + 20.7 \quad \text{for } 0 < S < 0.35. \quad (12)$$

The sheltering model is adopted locally wherever the above criterion is satisfied. Note that S is the wave steepness according to the experimental data, but it is replaced with the local surface slope in the numerical simulations in this study.

4.1.2. Wind-driven current

The presence of wind forcing introduces a thin surface drift layer, which may have important effects on the evolution of the wave groups [31,33]. This layer is of high vorticity and the velocity profile depends strongly on depth [33]; however, for simplicity, the layer may be modeled as a uniform surface current (e.g. [10]), which has a magnitude of typically a few percent of the wind

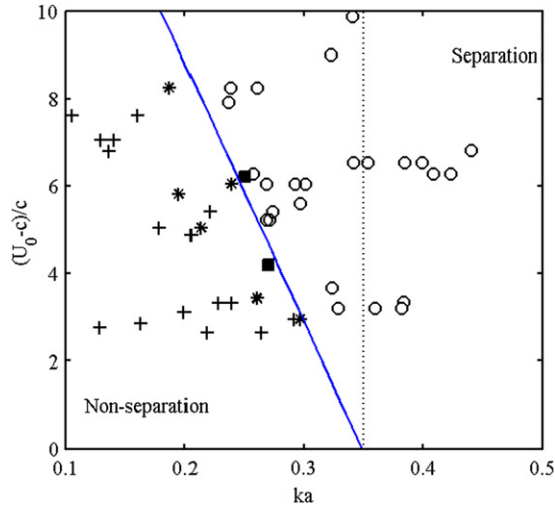


Fig. 6. Air flow separation criterion according to laboratory experiments and field measurements. The abscissa is wave steepness and the ordinate is non-dimensional relative speed. U_0 is the free stream wind speed and c indicates phase speed. Pluses: non-separation conditions; asterisks: conditions under which separation may or may not occur due to uncertainty in the flow visualization; circles: separation conditions; solid squares: separation conditions according to Donelan et al. [32]; dotted line: separation criterion used in [10]. The solid line indicates a linear least-squares fit of the Donelan data and Kharif data (lower limit). The best fit is used the air flow separation criterion in this study.

speed. For example, the measurement by Peirson and Banner [34] showed that the mean surface drift velocity is in the range of 1%–2%, depending on the measurement locations (i.e. fetch, wave trough and wave crest).

However, a uniform surface current speed, U_{cur} , is commonly assumed in numerical simulations. Kharif et al. [10] used a uniform surface current of 2% of the wind speed (i.e. $\gamma = U_{cur}/U_0 = 2\%$) in their study of wind influence on extreme wave events. Yan and Ma [27] conducted systematically numerical tests regarding a proper wind-driven current. They found that, depending on specific wind speed, $\gamma = 0.25 \sim 1\%$ produces satisfactory results and $\gamma = 0.5\%$ in general provides acceptable results for the predicted maximum surface elevation as a function of space for all cases considered. In our numerical simulations, we also include a uniform surface current to model the wind effects on the evolution of the wave groups. As discussed later, a wind-driven current of speed $\gamma \sim 1\%$ provides reasonable numerical results in comparison with our experimental measurements. Details can be found in the following sections.

4.2. Evolution of the wave groups under no wind action

Fig. 7(a) and (b) provide comparisons of the predicted and measured surface elevations for the non-breaking and breaking wave groups, respectively, in the absence of wind forcing. For the non-breaking wave group, the predicted surface elevations match well the measurement. For the breaking group, the prediction also agrees well with the experimental results, including the comparison downstream of the wave breaking region, which is located between the second and the third wave stations.

Since the surface elevation is predicted well with the wave breaking model, the spatial variation of the total energy is expected to be well predicted too. Fig. 7(c) shows the long time integration of the surface elevation squared, $\langle \zeta^2(t) \rangle$ which is proportional to the total energy passing a wave station according to linear wave theory. As expected, the total energy as a function of space for both non-breaking and breaking wave groups are predicted well in the simulations, though the energy dissipation due to wave breaking simulated with the eddy viscosity model appears slightly smaller

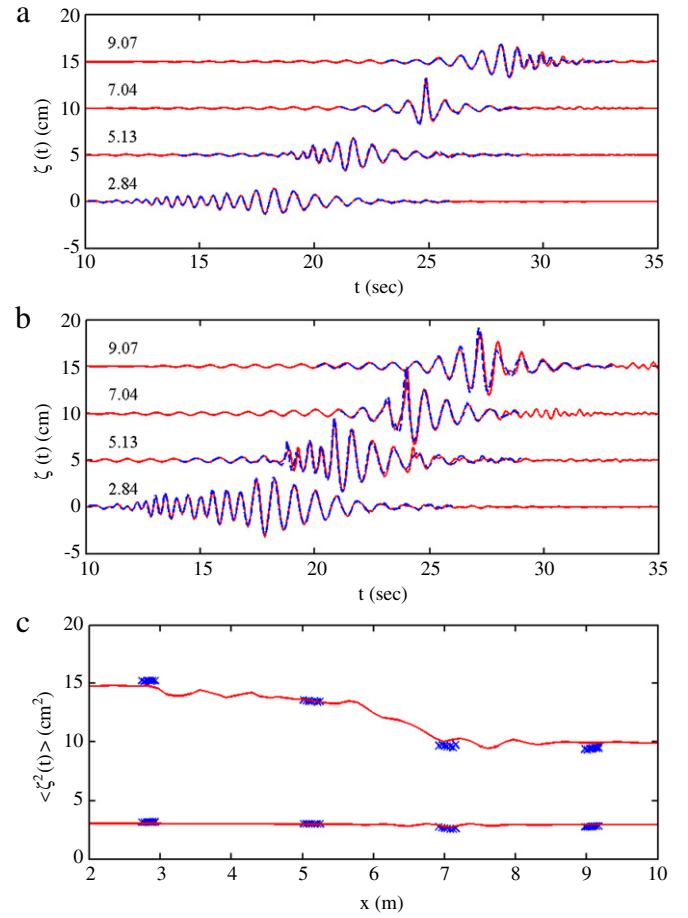


Fig. 7. Comparison of experimental and numerical results without wind forcing. (a) Surface elevation for non-breaking wave group DF 1; dashed lines: experiment; solid lines: simulation; measurement locations downstream of the wavemaker are indicated in the figure, e.g. 2.84 m. (b) Same as (a) but for breaking wave group DF 2; note that wave breaking occurs between the second and third wave stations. (c) $\langle \zeta^2(t) \rangle$ is the long time integration of surface elevation squared; crosses: experiment; solid lines: simulation.

than the measurement. Overall, the improved eddy viscosity model predicts well both energy dissipation in breaking events and the surface elevation downstream of breaking for the wave groups.

We now examine the wave spectrum of the dispersive focusing wave groups. Similarly, a good agreement of the wave frequency spectrum between the experimental and numerical results is expected. As shown in Fig. 8, the predicted amplitude spectra at different stations along the tank match well the measurements. In the evolution process, noticeable changes in wave spectrum for both the non-breaking and breaking wave groups are observed, which indicates that the dispersive focusing is far from linear superposition and it undergoes strong nonlinear process, consistent with the findings in [35].

In the previous study [35], compared to the experimental results, the magnitudes of the lower frequency wave components are found to be overestimated while the higher ones are underestimated in their numerical predictions. Tian et al. [35] attributed the discrepancy mainly to a relatively large effective kinematic viscosity introduced to account for the viscous related dissipation mainly due to friction on the wave tank (0.7 m wide) side walls and bottom. In this study, the wave tank is much wider (1.5 m) and a smaller effective kinematic viscosity is applied to the free surface to account for the viscous related dissipation. The good agreement shown in Fig. 8 confirmed that the discrepancy in the wave spectrum prediction in [35] is mainly due to the large effective kinematic viscosity used in their numerical simulations.

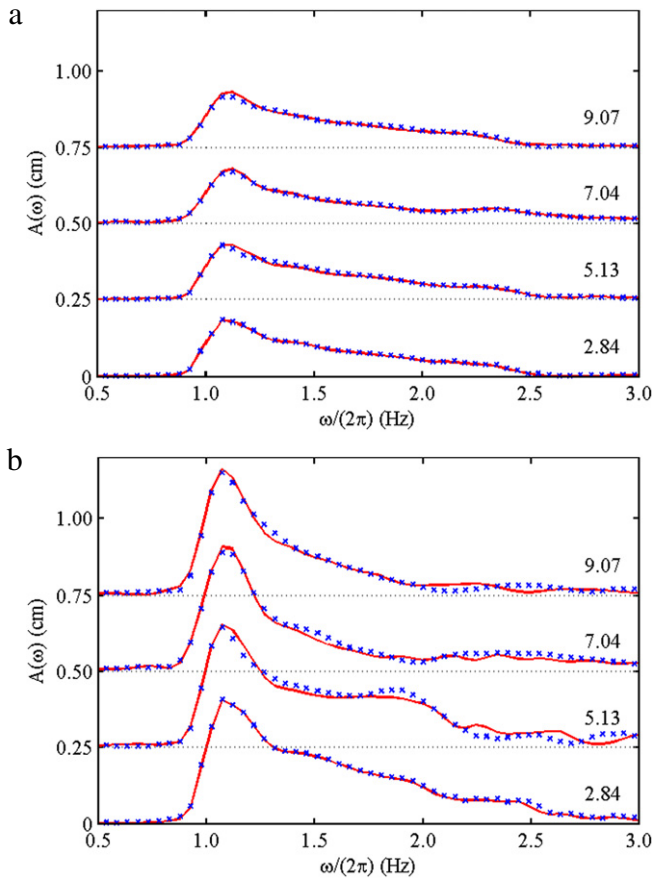


Fig. 8. Comparison of the amplitude spectrum for the groups under no wind forcing: (a) wave group DF 1 and (b) wave group DF 2. Crosses are from measurement and solid lines are computed with simulation results. The amplitude spectrum is defined as $A(f) = \frac{1}{T} \int_t^{t+T} \zeta(t) e^{-2\pi i f t} dt$. T is chosen long enough that the entire wave group is included within the duration. For clarity, an increment of 0.25 cm is applied to the ordinate to separate the amplitude spectrum at different wave stations.

4.3. Evolution of the wave groups under wind forcing

Fig. 9 provides the experimental and numerical results for the wave groups under wind forcing condition $U_0 = 1.4$ m/s. In the simulations, a uniform surface current has to be included to predict more accurately the evolution of the wave groups. We used three current speeds, i.e. $\gamma = U_{cur}/U_0 = 0.6\%$, 0.9% and 1.2% , and found that they produce numerical predictions close to each other in terms of both magnitude and phase. As shown in Fig. 9, despite some local disparities, the numerical models simulate well the evolution of the non-breaking and breaking wave groups under this weaker wind forcing condition (only the numerical results with $\gamma = 0.9\%$ shown). Note that an active breaking crest just occurs at the third station.

Comparisons of the numerical and experimental results for the wind condition $U_0 = 3.2$ m/s are provided in Fig. 10. As shown, local disparity in the comparison becomes more noticeable. Although not shown in the figure, we note that numerical predictions with $\gamma = 1.2\%$ appear to provide a better amplitude estimation while simulations with $\gamma = 0.6\%$ produce a better phase agreement, compared with the measurements in terms of both phase and amplitude. We also note that wind-generated waves can be observed far downstream in the experiments; however, we include no surface tension in the free surface boundary conditions and these short wind waves are not predicted well in the simulations.

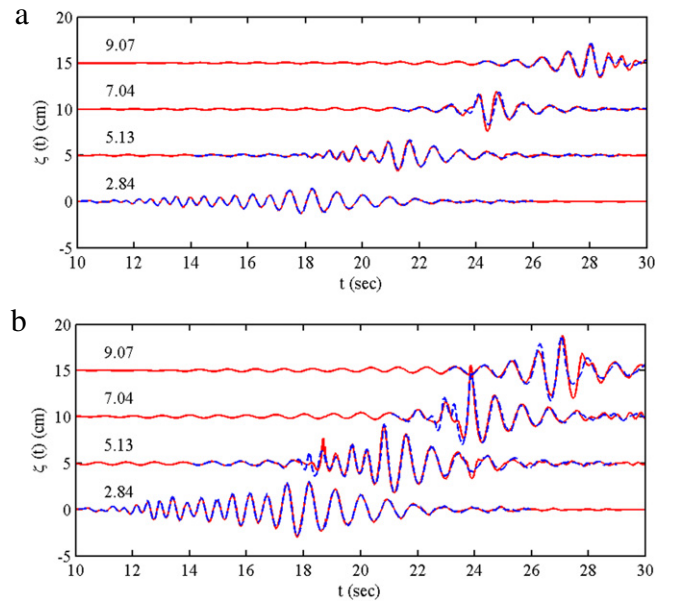


Fig. 9. Surface elevation of the wave groups under wind condition $U_0 = 1.4$ m/s: (a) the non-breaking group DF 1 and (b) the breaking group DF 2. Dashed lines: experiment; solid lines: numerical results with $\gamma = U_c/U_0 = 0.9\%$. The friction velocity used in the simulation is $u^* = 4.84$ cm/s (mean of the measurements at two fetches in Table 2).

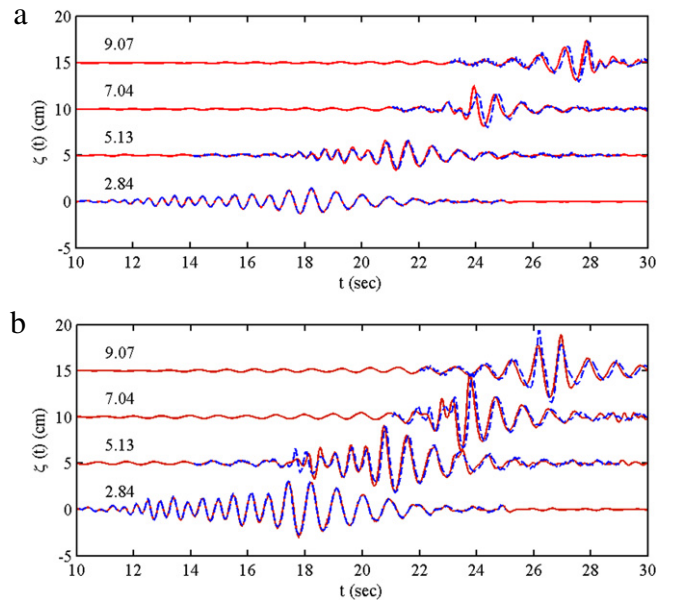


Fig. 10. Same as Fig. 9 but for wave groups under wind condition $U_0 = 3.2$ m/s. The friction velocity used in this simulation is $u^* = 12.7$ cm/s.

As the wind speed further increases to $U_0 = 5.0$ m/s, local disagreement between the simulation and the measurement becomes more evident, as shown in Fig. 11. It appears that the simulated surface elevation with $\gamma = 0.9\%$ demonstrates acceptable amplitude estimation although there is a small phase shift compared to the measurement. For the breaking group, an obvious disparity in the third wave station is observed and this disparity corresponds to an active breaking passing by the station. Note that an active plunging breaker also presents at the fourth wave station.

We also examined the measured and predicted maximum surface elevations as a function of space and the results are shown in Fig. 12. The numerical prediction matches well the measurement for the non-breaking wave group under no wind

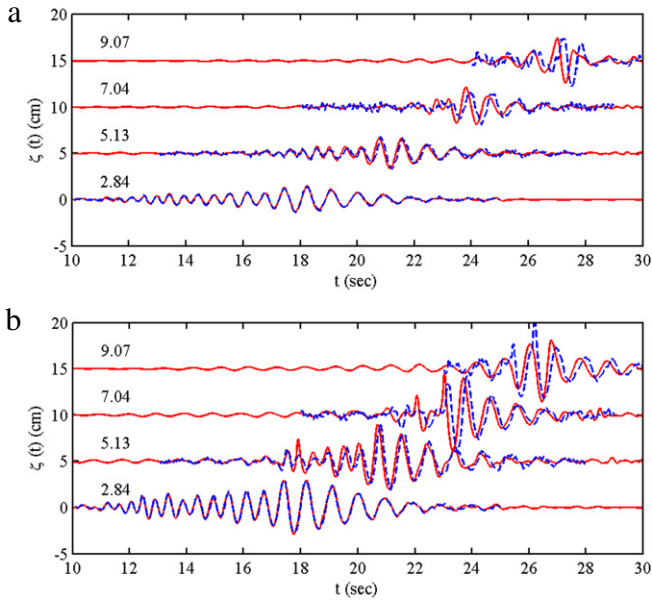


Fig. 11. Same as Fig. 9 but for wave groups under wind condition $U_0 = 5.0$ m/s. The friction velocity used in this simulation is $u^* = 22.2$ cm/s.

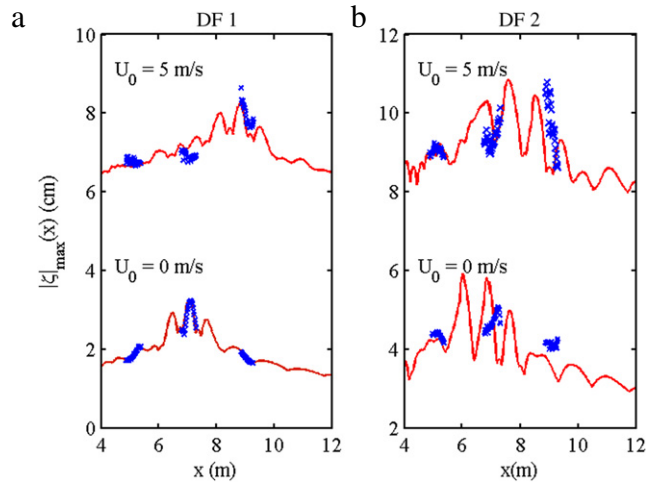


Fig. 12. Comparison of the measured (symbols) and the predicted (lines) maximum surface elevations for the non-breaking (a) and the breaking (b) wave groups. Crosses: experiment; solid lines: simulations with current speed $\gamma = 0.9\%$. For clarity, an offset of 5 cm is applied to the ordinate to separate the wind forcing case from the no wind action case.

action. The remaining comparisons are not so good, but still acceptable. Another obvious observation is that the wind forcing has delayed the wave focusing/breaking process and pushes the focusing/breaking point further downstream. Similar observations were reported in previous studies, e.g. [10]. They also showed that freak waves may be sustained longer by wind forcing (mainly air flow separation in the leeward of the extreme crests) and an asymmetric behavior of wave amplification in the focusing and defocusing processes. The results shown in Fig. 12 do not confirm their observations, possibly due to differences in wave group steepness, wind forcing condition, and forcing duration.

We make further comparisons by examining the spatial variation of the total wave energy, which is proportional to $\langle \zeta^2(t) \rangle$, and the results are shown in Fig. 13. In general, the total energy for both the non-breaking and breaking wave groups propagating under wind forcing is well predicted with the numerical models. The measured total energy at the fourth wave

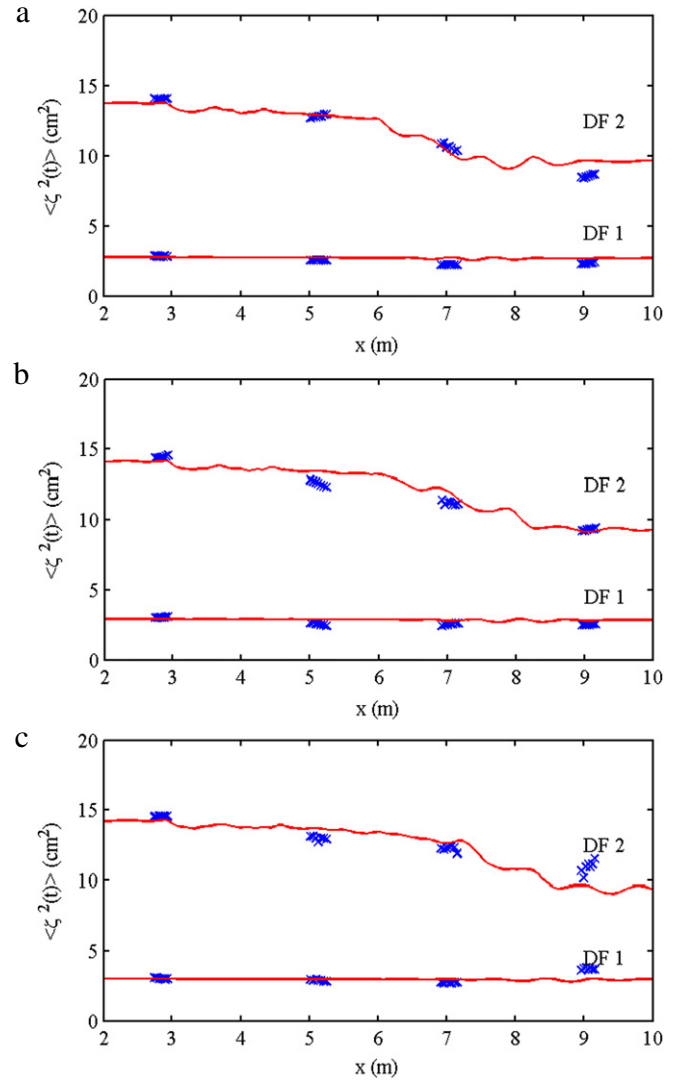


Fig. 13. Long time integration of surface elevation squared, $\langle \zeta^2(t) \rangle$, as a function of distance. (a) $U_0 = 1.4$ m/s, (b) $U_0 = 3.2$ m/s and (c) $U_0 = 5.0$ m/s. Crosses: experiment; solid lines: simulations with current speed $\gamma = 0.9\%$.

station for the strongest wind forcing case is higher than the numerical prediction, mainly due to the wind-generated waves in the experiments. Moreover, Fig. 14 presents a comparison of the measured and the predicted wave amplitude spectra for $U_0 = 3.2$ m/s. In general, the predictions at different locations along the tank agree well with the measurement, despite some discrepancy at the higher frequency wave components.

Overall, the disparity between the measured and the predicted surface elevations becomes more evident as the wind speed increases. However, when the wind-driven current is included in the simulation, the performance of the numerical models is reasonable for the weaker wind forcing conditions. It may also be regarded as acceptable for the strongest wind forcing condition, considering the simplicity of the wave breaking and the wind forcing models and the simplification made in the simulations, e.g. initial condition generation using only linear wave theory and the assumptions of constant wind speed, wind friction velocity, and wind-driven current speed in a given wind condition. For more accurate wave predictions under strong wind forcing conditions, these assumptions should be re-evaluated to develop a more realistic wind forcing model.

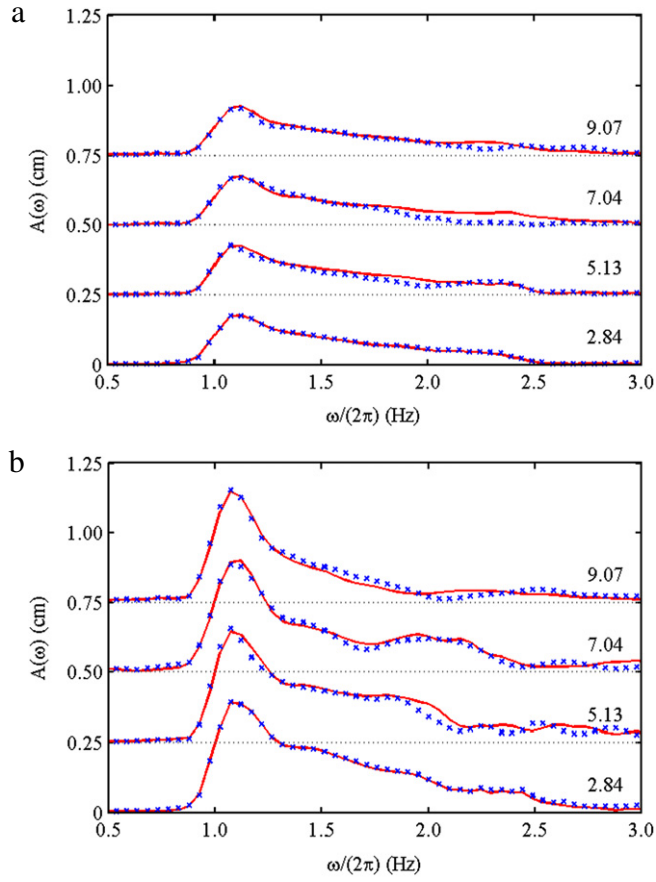


Fig. 14. Same as Fig. 8 but for comparison of the amplitude spectra for the groups under wind $U_0 = 3.2$ m/s: (a) wave group DF 1 and (b) wave group DF 2. Crosses are from measurement and solid lines are computed with simulation results ($\gamma = 0.9\%$).

4.4. Discussions

It is instructive to understand the roles of the two wind forcing models (i.e. Miles' and Jeffreys') on the evolution of focusing wave groups. For low steepness waves and weak wind forcing condition, air flow separation may not occur; therefore, Miles' model may be a model relevant to describe wind forcing effect. As the wave steepness and wind speed increase, air flow separation may occur more frequently. However, the separation is a highly unsteady process and may persist for only a short period [25,26] and, therefore, the overall effect due to flow separation on wave evolution may be less significant than expected. For example, Yan and Ma [27] found that the overall effect of air flow separation on the formation of freak waves may be neglected. However, Kharif et al. [10] argued that freak waves due to dispersive focusing may be sustained longer caused by air flow separation on the leeside of the extreme wave crests. Note that air flow may be fully separated over water waves and persist for a long duration under extreme wind conditions [32], but such conditions are beyond the scope of this study.

Here, we conduct additional numerical tests to investigate the effects of the two wind forcing models on the evolution of focusing wave groups under moderate wind forcing conditions. The numerical set-up is almost the same as that in Section 4.1 except for the following facts. First, the fifth-order model is solved throughout the numerical domain instead of dividing the domain into one linear and one nonlinear (fifth order) region. Second, the kinematic viscosity of water at room temperature ($\nu = 10^{-6}$ m²/s) instead of the equivalent viscosity ($\nu_{eqv} = 5 \times 10^{-6}$ m²/s) is used

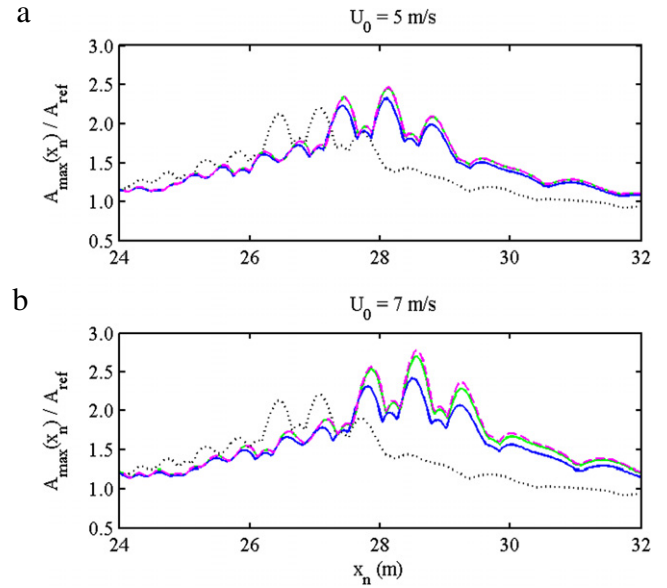


Fig. 15. Wave amplitude amplification factors under two wind conditions. Dotted lines: no wind forcing; blue solid lines: Jeffreys' sheltering model; green solid lines: Miles' model; dashed lines: the combined model used in this study.

to minimize the non-breaking dissipation effect. Third, the wind forcing is applied throughout the numerical domain to achieve relatively long wind forcing period; the friction velocity is assumed to be 5% of the wind speed and the wind-driven current speed is taken as $\gamma = 0.9\%$. The initial condition is generated from the non-breaking wave group.

Fig. 15 shows the amplitude amplification factor, $A_{max}(x_n)/A_{ref}$, as a function of space for the wave group under four numerical wind forcing conditions: no wind, Miles' model, Jeffreys' sheltering model, and a combined Miles and Jeffreys' model. Here, $A_{max}(x_n)$ is the maximum surface elevation predicted at location x_n in the numerical wave tank and A_{ref} is a reference amplitude, which is taken as the average maximum surface elevation observed between $x_n = 22$ m–22.5 m. As shown, the wind delays the wave focusing and pushes it further downstream. The maximum amplification factor achieved under wind action is greater than that under no wind forcing. In addition, Miles' mechanism produces greater increment in the amplification factor than the Jeffreys' sheltering model for both wind forcing conditions ($U_0 = 5$ m/s and 7 m/s).

Fig. 16 presents the total potential energy growth as a function of time in the numerical wave tank. Under no wind action, the energy decreases slightly due to viscosity. In the wind condition of $U_0 = 5$ m/s, Miles' model produces significant energy transfer from wind to the wave group; on the other hand, air flow separation is predicted, but the overall contribution due to the sheltering mechanism to wave energy growth is minimal. The combined model, therefore, provides results close to that of Miles' model. When the wind speed increases to 7 m/s, similar observations for Miles' and Jeffreys' models are made. However, when the two models are combined, the overall energy transferred to the wave group is much greater than the simple summation of those due to the two separate mechanisms. In the focusing stage, Miles' model is responsible for the wave energy growth; in the vicinity of the focusing point, the waves become strongly nonlinear and, under strong wind forcing, air flow separation may occur continuously. The sheltering mechanism then contributes greatly to the wave energy growth.

According to this numerical investigation, one may argue that Miles' model may be considered proper for waves of moderate

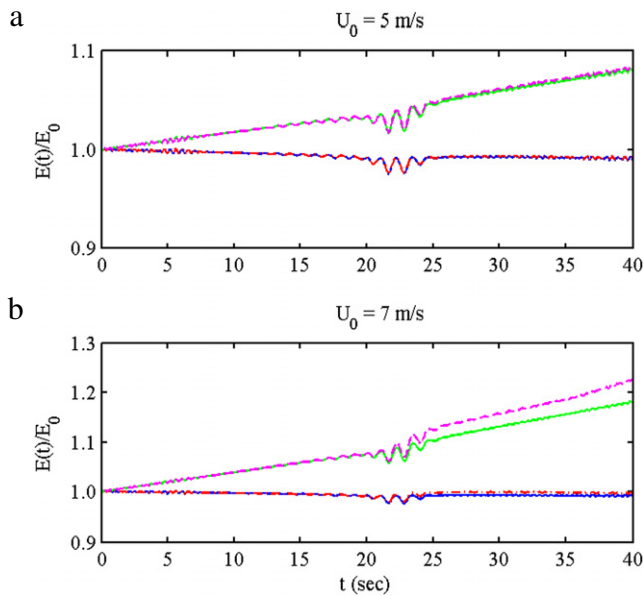


Fig. 16. Total potential energy as a function of time in the numerical wave tank. Blue solid lines: no wind action (for reference); red dash-dotted lines: Jeffreys' model only; green solid lines: Miles' model only; pink dashed lines: the combined model.

steepness under weak to moderate wind forcing; however, for high steep waves under strong wind forcing, both Miles' and Jeffreys' mechanisms may have to be considered. Note that Peirson and Garcia [36] showed that the growth rate parameter, β , decreases systematically with increase wave steepness. In this study, a constant β is used, which may affect the relative importance of the two wind forcing models. This should be an issue to be considered in future studies.

The scalability and applicability of the numerical models, as well as the proposed air flow separation criterion, to longer waves and broader wave spectra (oceanic waves) should be examined carefully. However, detailed studies on the problem are non-trivial due to the limitation of the experimental facilities and the complicated physical processes involved. Collaborative work involving rigorous theoretical analysis, high performance numerical computations, and high quality field measurements are necessary to improve our understanding of the problem.

5. Conclusions

The evolution of two-dimensional dispersive focusing wave groups in deep water under wind forcing and wave breaking effects is investigated numerically using a wave prediction model based on a pseudo-spectral method. In addition, two-dimensional wind-wave experiments are conducted and surface elevations at different wave stations along the tank are measured with high-speed imaging. Detailed measurements of the wind conditions are also performed. These measurements are used to evaluate the performance of the numerical models. It is found that the numerical model produces acceptable predictions for the evolution of the wave groups under the breaking and the wind forcing conditions considered in this study.

In the numerical simulations, to model breaking waves, an eddy viscosity model is incorporated into a system of nonlinear evolution equations for the surface elevation and the free surface velocity potential to simulate energy dissipation due to wave breaking and predict surface elevations after breaking. Wind forcing is modeled by introducing a surface slope coherent pressure distribution in the dynamic free surface boundary

condition. The pressure term is expressed through Miles' shear flow instability theory and Jeffreys' sheltering theory. To apply the two mechanisms to waves under wind forcing, i.e. a combined wind forcing model, an air flow separation criterion depending on wind speed and wave steepness is proposed based on laboratory experiments and field observations. In addition, it is found that wind-driven current has to be considered in the simulation of wave evolution under wind forcing. For the waves and wind forcing considered in this study, the magnitude of wind-driven current being 0.9% of the wind speed produces reasonable predictions.

Direct comparisons of the experimental measurements and the numerical simulations are made. For wave groups under no wind action, the eddy viscosity model simulates well the energy dissipated in breaking waves and predicts well the surface elevation after breaking. The predicted wave spectra before and after breaking also agree well with the measurements. Under the weaker wind forcing condition, the combined wind forcing model, after consideration of the wind-driven current, produces satisfying prediction. As the wind forcing becomes stronger, the disparity between the experiments and the simulations becomes more evident, but the numerical results are still regarded as acceptable, considering the use of the relatively simple wave breaking and wind forcing models.

The relative importance of Miles' and the Jeffreys' models are discussed through additional numerical investigations. It is shown that Miles' model may be considered appropriate for waves of moderate steepness under weak to moderate wind forcing; however, for high steep waves under strong wind forcing, both Miles' and Jeffreys' mechanisms may have to be considered.

The wind forcing and wave breaking models considered in this study still need to be improved considerably for oceanic applications since these models have been developed for long-crested waves by assuming airflows are laminar or, at least, neglecting turbulent fluctuations in wind. Therefore, we stress that care must be taken when our findings are applied to real ocean conditions as the spatial and temporal scales of turbulence in the ocean are so different from those in a laboratory, in addition to three-dimensionality of real ocean waves. For a better description of wave growth and breaking of ocean waves in wind, we should develop a wave model with a parameterization for breaking of short-crested waves along with a turbulent closure model valid for a wide range of spatial and temporal scales. Although far from complete, the present study is expected to help in development of such a model.

Acknowledgments

The authors gratefully acknowledge the support from the Korea Science and Engineering Foundation through the WCU program (Grant No. R31-2008-000-10045-0).

References

- [1] G. Wu, Direct simulation and deterministic prediction of large-scale nonlinear ocean wave-field, in: Ph.D. Dissertation, Massachusetts Institute of Technology, 2004.
- [2] A. Kalmikov, Modeling wind forcing in phase resolving simulation of nonlinear wind waves, in: Ph.D. Dissertation, Massachusetts Institute of Technology, 2010.
- [3] B.J. West, K.A. Brueckner, R.S. Janda, D.M. Milder, R.L. Milton, A new numerical method for surface hydrodynamics, *J. Geophys. Res.* 92 (1987) 11803–11824.
- [4] W. Bateman, C. Swan, P. Taylor, On the efficient numerical simulation of directionally spread surface water waves, *J. Comput. Phys.* 174 (2001) 277–305.
- [5] Z.G. Tian, M. Perlin, W. Choi, Evaluation of a deep-water wave breaking criterion, *Phys. Fluids* 20 (2008) 066604.
- [6] A. Goullet, W. Choi, Nonlinear evolution of irregular surface waves: comparison of numerical solutions with laboratory experiments for long crested waves, *Phys. Fluids* 23 (2011) 016601.

- [7] Z. Tian, M. Perlin, W. Choi, Energy dissipation in two-dimensional unsteady plunging breakers and an eddy viscosity model, *J. Fluid Mech.* 655 (2010) 217–257.
- [8] Z. Tian, M. Perlin, W. Choi, An eddy viscosity model for two-dimensional breaking waves and its validation with laboratory experiments, *Phys. Fluids* 24 (3) (2012) 036601.
- [9] J. Touboul, J.P. Giovanangeli, C. Kharif, E. Pelinovsky, Freak waves under the action of wind: experiments and simulations, *Eur. J. Mech. B/Fluids* 25 (2006) 662–676.
- [10] C. Kharif, J.P. Giovanangeli, J. Touboul, L. Grare, E. Pelinovsky, Influence of wind on extreme wave events: experimental and numerical approaches, *J. Fluid Mech.* 594 (2008) 209–247.
- [11] M.L. Banner, J. Song, On determining the onset and strength of breaking for deep water waves. Part II: influence of wind forcing and surface shear, *J. Phys. Oceanogr.* 32 (2002) 2559–2570.
- [12] J.W. Miles, On the generation of surface waves by shear flows, *J. Fluid. Mech.* 3 (1957) 185–204.
- [13] H. Jeffreys, On the formation of water waves by wind, *Proc. Royal Soc. London. Series A* 107 (1925) 189–206.
- [14] S. Yan, Q.W. Ma, Numerical simulation of interaction between wind and 2-D freak waves, *Eur. J. Mech. B/Fluids* 29 (2010) 18–31.
- [15] J. Wu, Laboratory studies of wind–wave interactions, *Tellus* 21 (1969) 708–713.
- [16] M.L. Banner, W.K. Melville, On the separation of air flow over water waves, *J. Fluid Mech.* 77 (1976) 825–842.
- [17] S. Kawai, Visualization of airflow separation over wind–wave crests under moderate wind, *Boundary-Layer Meteorol.* 21 (1981) 93–104.
- [18] M.A. Weissman, Observations and measurements of air flow over water waves, in: O.M. Phillips, K. Hasselmann (Eds.), *Wave dynamics and radio probing of the ocean surface*, Chapter 23, Plenum Press, New York, 1986, pp. 225–253.
- [19] W. Craig, C. Sulem, Numerical simulation of gravity waves, *J. Comput. Phys.* 108 (1993) 73–83.
- [20] W. Choi, Nonlinear evolution equations for two-dimensional surface waves in a fluid of finite depth, *J. Fluid Mech.* 295 (1995) 381–394.
- [21] D.A. Drazen, W.K. Melville, L. Lenain, Inertial scaling of dissipation in unsteady breaking waves, *J. Fluid Mech.* 611 (2008) 307–332.
- [22] D.A. Drazen, W.K. Melville, Turbulence and mixing in unsteady breaking surface waves, *J. Fluid Mech.* 628 (2009) 85–119.
- [23] J. Touboul, C. Kharif, On the interaction of wind and extreme gravity waves due to modulational instability, *Phys. Fluids* 18 (10) (2006) 108103.
- [24] W.J. Plant, J.W. Wright, Growth and equilibrium of short gravity waves in a wind–wave tank, *J. Fluid Mech.* 82 (1977) 767–793.
- [25] N. Reul, H. Branger, J.P. Giovanangeli, Air flow separation over unsteady breaking waves, *Phys. Fluids* 11 (1999) 1959–1961.
- [26] N. Reul, H. Branger, J.P. Giovanangeli, Air flow structure over short-gravity breaking water waves, *Boundary-Layer Meteorol.* 126 (2008) 477–505.
- [27] S. Yan, Q.W. Ma, Improved model for air pressure due to wind on 2D freak waves in finite depth, *Eur. J. Mech. B/Fluids* 30 (2011) 1–11.
- [28] Z. Tian, M. Perlin, W. Choi, Observation of the occurrence of air flow separation over water waves, *Proc. 29th Inter. Conf. on Ocean, Offshore and Arctic Eng.* 4 (2010) 333–341.
- [29] M.L. Banner, The influence of wave breaking on the surface pressure distribution in wind–wave interactions, *J. Fluid Mech.* 211 (1990) 463–495.
- [30] D. Dommermuth, The initialization of nonlinear waves using an adjustment scheme, *Wave Motion* 32 (2000) 307–317.
- [31] M.L. Banner, M. Phillips, On the incipient breaking of small scale waves, *J. Fluid Mech.* 65 (1974) 647–656.
- [32] M.A. Donelan, A.V. Babnin, I.R. Young, M.L. Banner, Wave-follower field measurements of the wind-input spectral function. Part II: parameterization of the wind input, *J. Phys. Oceanogr.* 36 (2006) 1672–1689.
- [33] O.M. Phillips, M.L. Banner, Wave breaking in the presence of wind drift and swell, *J. Fluid Mech.* 66 (1974) 625–640.
- [34] W.L. Peirson, M.L. Banner, Aqueous surface layer flows induced by microscale breaking wind waves, *J. Fluid Mech.* 479 (2003) 1–38.
- [35] Z. Tian, M. Perlin, W. Choi, Frequency spectra evolution of two-dimensional focusing wave groups in finite depth water, *J. Fluid Mech.* 688 (2011) 169–194.
- [36] W.L. Peirson, A.W. Garcia, On the wind-induced growth of slow water waves of finite steepness, *J. Fluid Mech.* 608 (2008) 243–274.